CORE
Metadata, citation and similar papers at core.ac.uk
Provided by Queen Mary Research Online

Lignin-derived electrospun freestanding carbons as alternative electrodes for redox flow batteries

Maria Crespo Ribadeneyra,[a],[b] Lia Grogan,[c] Heather Au,[d] Philipp Schlee,[a],[b],[d] Servann Herou,[a],[b],[d] Tobias Neville,[e] Patrick L. Cullen,[e] Matt D. R. Kok,[e] Omid Hosseinaei,[f] Sverker Danielsson,[f] Per Tomani,[f] M. M. Titirici,[d] Daniel J. L. Brett,[e] Paul R. Shearing,[e] Rhodri Jervis*[e] and Ana Belen Jorge* [a],[b]

[a] Queen Mary University of London, School of Engineering and Materials Science, Mile End Road, E1 4NS, London, UK

[b] Materials Research Institute, Queen Mary University of London, Mile End Road, E1 4NS, London, UK

[c] Trinity College Dublin, The University of Dublin, College Green, Dublin 2, D02 PN40, Ireland

[d] Imperial College London, Department of Chemical Engineering, South Kensington Campus, SW7 2AZ, UK

[e] Electrochemical Innovation Lab, Department of Chemical Engineering, University College London, Torrington Place, WC1E 7JE, London, UK

[f] RISE (Research Institutes of Sweden), Drottning Kristinas väg 61, Stockholm, Sweden

Abstract

Redox flow batteries represent a remarkable alternative for grid-scale energy storage. They commonly employ carbon felts or carbon papers, which suffer from low activity towards the redox reactions involved, leading to poor performance. Here we propose the use of electrospun freestanding carbon materials derived from lignin as alternative sustainable electrodes for all-vanadium flow batteries. The lignin-derived carbon electrospun mats exhibited a higher activity towards the

*Corresponding authors. Tel: +44 (0)20 7882 6782. E-mail: a.sobrido@qmul.ac.uk (Ana Belen Jorge Sobrido). Tel: +44(0)2076797233. Email: rhodri.jervis@ucl.ac.uk (Rhodri Jervis)

VO_2^+/VO^{2+} reaction than commercial carbon papers when tested in a three-electrode electrochemical cell (or half-cell), which we attribute to the higher surface area and higher amount of oxygen functional groups at the surface. The electrospun carbon electrodes also showed performance comparable to commercial carbon papers, when tested in a full cell configuration. The modification of the surface chemistry with the addition of phosphorous produced different effect in both samples, which needs further investigation. This work demonstrates for the first time the application of sustainably produced electrospun lignin-derived carbon electrodes in a redox flow cell, with comparable performance to commercial materials and establishes the great potential of biomass-derived carbons in energy devices.

1. Introduction

It is now a widely accepted scientific fact that anthropogenic climate change will cause catastrophic damage in the very near future, as CO_2 concentrations have increased by 40% since pre-industrial times. In addition, the most recent Intergovernmental Panel on Climate Change (IPCC) report established that global temperatures are rising and the number of unusual climate phenomena observed since the 1950s are unprecedented[1]. This stems primarily from fossil fuel emissions. It is thus clear that a move away from dependence on fossil fuels is critical. However, electricity from sustainable energy sources is generated sporadically, unevenly and in a decentralized fashion. Existing electrical grids were never designed with this type of energy production in mind[2]. Where conventional power plants produce stable amounts of power over an extended period, in the case of solar and wind power, energy demand often diverges from energy production[3]. To enable the continuous supply of electricity, we must redesign the grid by combining inconsecutive renewable power sources and large-scale energy storage systems.

Redox flow batteries (RFBs) have, thus far, showed great potential for large-scale stationary storage technology[3][4]. RFBs convert chemical energy into electrical energy directly, they are readily

scalable and versatile, and hold an advantage over conventional batteries as they allow for independent scaling of power and capacity. Additionally, as they do not employ the intercalation reactions of Li-ion batteries, there is no morphological change to the electrode on charge/discharge and therefore do not suffer from the same capacity fade mechanisms, providing them with potentially longer lifetimes. Amongst RFBs, the all-vanadium redox flow battery (VRFB) has been the most successful and implemented on a commercial scale by a variety of companies[5][6] due to multiple key characteristics (e.g. safety, large power output and storage capacity, rapid response, elongated cycle life, high efficiency, minimal cross-contamination and environmental compatibility[7][8]). VRFBs utilize vanadium ions with different oxidation states as active species in two half-cell electrolyte reservoirs to store electrical energy. The power of the system is determined by the rate of the reaction of the redox species at each electrode, which is the crucial component of the battery, as it provides the reaction sites for the relevant redox couples. Therefore, an important aim of the optimization and development of novel electrodes is to enhance the electrocatalytic activity towards vanadium V^{3+}/V^{2+} and VO_2^{+}/VO^{2+} reactions, since this can hugely improve the efficiency and reduce the cost of the system[9][10].

The efficiency of the electrode will affect the cell performance as it has an influence on cell voltage losses associated with activation overpotential, concentration overpotential and ohmic losses[11]. RFB electrodes act as the reaction sites for the redox reactions taking place in the electrolyte, as well as the porous media through which it flows, and therefore their microstructural and electronic properties have a strong influence on polarization losses in the cell[10]. Minimization of polarization in the electrode should be sought after in order to achieve maximum battery efficiency. Therefore, an ideal electrode material must enable fast kinetics for the redox couple while inhibiting undesirable side reactions such as the hydrogen evolution reaction (HER). Additionally, high surface area, porosity and permeability, mechanical and chemical durability and high electrical conductivity are properties that an efficient electrode should possess. Thus far, carbon materials such as graphite felts and papers have been mainly used as electrode materials in VRFBs due to their high electrical

conductivity, good stability, corrosion resistance and their wide range for operating potentials[12]. These materials, however, are usually derived from polyacrylonitrile (PAN) and processed at high temperatures. Furthermore, these electrodes normally present poor electrochemical activity and wettability,[13] while high cost is also a large-scale limitation[14]. Thus, the need for cost effective and mass-produced electrodes with tuneable properties has encouraged research on biomass-derived materials for VRFBs[7][15]. Renewable precursors for electrodes are of high interest as they are abundant and cheap, as well as providing multiple chemical functionalities of great interest for the design of functional carbon nanomaterials[16][17]. Lignin as a biomaterial presents itself as an appealing precursor for fibrous electrodes as it is a cheap, plentiful waste product of the paper industry and contains an abundance of the desired functional groups[18][19][20].

Here we propose and test an electrode for all-vanadium redox flow batteries derived from lignin. We propose the up-cycle of lignin into high surface area cheap battery electrodes through electrospinning, which is an efficient and tunable process with a record of successful implementation in producing nanofibers, and recently for application in RFBs[21][22][23]. For the sake of comparison, a commercially available fibrous carbon analogue has been also tested.

2. Experimental Section

2.1 Lignin isolation and electrospinning

Softwood kraft lignin was obtained from a LignoBoost process (Bäckhammer, Sweden). A sequential solvent extraction was used to produce the suitable lignin fraction for electrospinning of lignin. The solvent extraction method was a simplified version of the method described elsewhere[24][25]. In brief, the dry lignin was first extracted with methanol, by rapidly stirring in 10 L methanol at room temperature for 2 h. The sample was filtrated and the solid recovered on the filter was then extracted using a 70/30 v/v mixture of methanol and methylene chloride (1:10 solid to liquid ratio, room temperature, 4 h). The extract solution was then filtered, and lignin from the filtrate was isolated using

a rotary evaporator. The isolated lignin was dried in a vacuum oven at 80°C for 12 h and then was used for electrospinning. The final yield for this fraction was 42.5%.

Electrospinning solution was prepared by dissolving the lignin in DMF at concentration of 47 wt%. The dope solution was placed in a 5 mL BD plastic syringe and was fed to a 22G flat-tipped syringe needle (Hamilton) using a Kd Scientific pump at a rate of 0.5 mL/h. A grounded cylinder (10 cm in diameter, 18 cm in width) covered by aluminum foil and rotating at 60 rpm was used as the collector. The distance between the needle tip and the collector was 17 cm. A Glassman high voltage power supply was used to generate an electrical field of 17 kV between the needle and collector. The submicron fibers, as nonwoven mat, were collected on the surface of aluminum foil at room temperature.

The as-spun lignin fiber mats were converted to carbon fiber mats by a two-step thermal treatment. In the first step, lignin fibers were oxidatively thermostabilized by heating the samples to 250°C at a rate of 0.5°C/min and then holding for 30 min at 250°C in a MTI Box Furnace (KSL-1200X), under an air flow of 10L/min.

2.2 Preparation of electrodes

The previously thermostabilized lignin fiber mats were cut into strips and carbonized between two pieces of Alfa Aesar® carbon felt (3.18 mm thick, 99.0 %, 2.4 g/10x10 cm) in a MTI 1200x tubular furnace at 800 °C during 2h, using a heating rate of 3˚C/min and a nitrogen flow rate of 0.5 L/min.

Commercial Sigracet® GDL 29AA non-woven carbon fiber fabric sheet (SGL group, thickness: 180 μm ±30) was used as-received, without any additional treatment, as a reference material for the sake of comparison. P-doped materials were prepared following a previously reported protocol[26]. Briefly, 2.5×2.5 cm^2 samples of either our electrospun mats (CNF) or the Sigracet® carbon fiber sheets (GDL29AA) were degassed in vacuum and a 2M solution of Ammonium hexafluorophosphate (NH_4PF_6, 99.98 % Sigma Aldrich) was slowly introduced until the material had been completely covered by the liquid. Vacuum was maintained for 5 min to ensure the complete infiltration of the

NH_4PF_6 solution into the pores of materials. After this time, samples were taken from the solution allowing the excess of liquid to drip onto a filter paper. Samples were carefully dried in a vacuum oven at 100 °C overnight and then annealed for 2 h at 500 °C using a heating rate of 3 ˚C/min.

2.3 Electrochemical measurements

Electrochemical measurements were done with a VSP Bio-Logic potentiostat/galvanostat. Cyclic voltammetry (CV) was performed at 10 mVs^{-1} between -0.3V and 1.2 V in a three-electrode cell configuration and using a 0.05M $V^{3+/}VO^{2+}$ commercial electrolyte solution (originally supplied in a 1.6 M $V^{3+/}VO^{2+}$ concentration in 3M H_2SO_4 and 0.5 M H_3PO_4 by Oxkem, UK). In this setup, a KCl saturated calomel Hg_2Cl_2 electrode (SCE) and a Pt coil were used as reference and counter electrodes, respectively. Working electrodes (pristine or P-doped electrospun mats or Sigracet® carbon fiber sheets) were punched with a diameter of 1cm and exposed to the electrolyte solution by inserting the thin samples (150-250 μm) between two PTFE holders; the front one having a 0.9 cm∅ circular opening provided with an inner 1 cm∅ Pt ring (current collector) and a solid back one as support. Before assembling the cell, the electrodes were wetted by adding a few drops of electrolyte on the electrode and pressing it.

Our VRFB cell (GGM Engineering, UK) consists of two metallic current collectors, two graphite flow plates and two 2.18mm thick PTFE frames with a 2.25×2.25 cm central opening where the thin (200-250 μm thick, size fitted to the frame opening 2.25×2.25 cm) CNF or GDL 29AA electrodes are placed on top of a 3.18mm thick Alfa Aesar® carbon felt (2.25×2.25 cm piece) that was thermally annealed at 1000 °C for 2 h prior usage. The samples, mounted in the PTFE frames, are then separated by a Nafion® membrane (115, 0.005 in. thick, DuPont de Nemours & Co) with the materials to be tested placed next to the membrane. 20 ml of the $V^{3+/}VO^{2+}$ 1.6M commercial electrolyte solution (Oxkem) was used on each side of the battery and recirculated at 30 mL min^{-1} using a two-channel peristaltic pump (323 Watson-Marlow). The battery was then pre-charged at 200 mA until reaching a voltage of 1.7V and subsequently maintained at this voltage until the current density had dropped

below 4 mA cm^{-2}(100% SOC). At this stage, Vanadium species have been totally converted to VO_2^{2+} (yellow) in the cathode and to V^{2+} in the anode (violet). To determine cell power performance, Galvanostatic polarization curves between 20 and 900 mA were recorded by screening the voltage drop observed in the battery when subjected to a steady current density for 30 s. Between each current density holding step, the battery was recharged at 10 mA cm^{-2} to assure a starting point of 100% SOC for each point on the polarization curve. Immediately after, cell cycling was performed at a constant current density of 40 mA cm^{-2} for 15 charge-discharge cycles between 0.7 and 1.7 V as potential limitations for discharge and charge steps, respectively. Electrochemical impedance spectroscopy (EIS) was performed before and after both polarisation and cycling experiments between 500kHz and 10mHz with a signal amplitude of 5mV to ensure the cell resistance remained unaltered after each sweep.

2.4 Characterization

Samples were analysed by nitrogen and CO_2 sorption measurements in liquid nitrogen (77K) and in an ice bath using Autosorb iQ (Quantachrome) to determine the pore structure and the Brunauer Emmett Teller (BET) surface area. The pore size distribution (PSD) is calculated from the adsorption isotherm using a quenched-solid model QSDFT assuming slit and cylindrical pore geometries.

The morphological analysis of samples was done through Scanning Electron Microscopy on a FEI Inspect F instrument. X-ray photoelectron spectroscopy data were recorded using a ThermoFisher Nexsa X-ray spectrometer equipped with an Al Kα monochromated X-ray source. Survey scans were acquired using 200 eV pass energy, 1 eV step size and 200 ms (10 ms x 20 scans) dwell times. C1s and O1s spectra were acquired using 50 eV pass energy, 0.1 eV step size and 1 s (100 ms x 10 scans) dwell times. P 2p spectra were acquired using 50 eV pass energy, 0.1 eV step size and 3 s (100 ms x 30 scans) dwell times. Pressure during measurement acquisition was $\leq 1 \times 10^{-9}$ mbar. Atomic compositions were calculated from averaged spectra obtained from 3 areas per sample.

Raman spectroscopy measurements were done with a Renishaw Ramanscope using a laser line of 633

nm. Spectra were recorded in three different spots per sample, using 50% of the laser power and taking three-30 s acquisitions. Deconvolution of peaks was done using the Renishaw's WiRE software.

Electrical conductivity of materials was measured at 30% of compression and perpendicular to the plane of the mats, to mimic the state at which electrodes perform in the RFB cell. Two point-probe resistance was recorded by placing the 5.06 cm^2 Sigracet/CNF layer (200-250 μm thick) on top of the Alfa Aesar® carbon felt (3.18 mm thick) and then both layers within the PTFE frame (2.18 mm). Two gold-coated plates were placed by each side of the frame and tightly compressed. Conductivity of materials was calculated from the measured resistance across the gold-coated plates, and considering an area of 5.06 cm^2 and a thickness of 0.218 cm.

Imaging of the GDL 29AA material was conducted using a Zeiss Xradia Versa 520 micro-CT instrument (Carl Zeiss XRM, Pleasanton, CA), operating with a source voltage of 40 kV. 1601 projections of 5 s exposure each were recorded through an angular sample rotation of 360^0. Reconstruction of the X-ray transmission images was conducted using a filtered back-projection reconstruction algorithm (XM Reconstructor, Zeiss). Use of a 20x objective lens and pixel binning of 1 yielded a voxel size of 0.37 μm in the reconstructed 3D data.

Due to the small fibers in the CNF material, nano-CT was required to give sufficient resolution to resolve the fiber detail, as described previously [22]. Additionally, to get a more detailed view of the structure of the carbon particles in the void of the GDL, it was also scanned at higher resolution in the nano-CT. A lab-based nano-CT instrument (Zeiss Xradia Ultra 810, Carl Zeiss Inc., Pleasanton, CA) was used to acquire the X-ray images, containing a Cr anode source with an accelerating voltage of 35 kV, producing a quasi-monochromatic beam at the Cr-Kα emission line of 5.4 eV. A Fresnel zone plate was employed as the objective element to produce a magnified image on a 1024^2 pixel CCD detector and images were acquired in large field-of-view mode with no binning, resulting in a pixel size of ca. 63 nm and a field-of-view of ca. 65 μm. The sample was rotated through 180^0 and

radiographs collected at discrete angular intervals, the parameters can be found in [21]. The radiographs were then reconstructed with proprietary software (XMReconstructor, Carl Zeiss Inc.) using a parallel beam reconstruction algorithm. Each electrode was scanned in Zernike phase contrast mode where an Au phase ring is inserted in the back focal plane of the objective and shifts the un-diffracted component of the beam, resulting in negative Zernike phase contrast (more details in [27]. The CNF sample was also scanned in absorption contrast mode and combined with the phase contrast image using Dual Scan Contrast Visualizer software (Zeiss) with a 50/50 contribution from each image using a method described by Taiwo et al. [28]. The segmented data sets were used to calculate the void volume fraction and tortuosity of the material using a random walk simulation, as well as the fiber and pore diameter, using the local thickness method described in [21]. Due to the delamination experienced in the CNF sample, a sub volume was used for these calculations, which can be seen in Figure S1d.

3. Results and Discussion

3.1 Characterization

As summarized in Figure 1a, the aim of this work is to compare a lignin-derived electrospun carbon nanofiber mat (CNF) with a commercially available carbon paper (GDL29AA, Sigracet®) as fibrous electrodes for a VRFB. When comparing both samples in their pristine form, we can observe that fibers of GDL29AA are clearly much thicker (*ca.* 10µm) than those of CNF (0.9-1µm) and therefore the bulk CNF material exhibits a denser structure, with smaller void spaces between fibers (Figures 1b and 1c) from SEM. The BET surface area for CNF is ~14 times that of GDL29AA (742 *vs.* 41 m^2 g^{-1}, see Tables S1 and S2 in SI), despite of the flaky features that can be found within the interstices of the latter (Figure 1b), which reveals that the electrospinning of lignin leads to meso / microporous freestanding mats.

Since lignin is an oxygen rich precursor, it is not surprising that the X-ray photoelectron spectroscopy

(XPS) results reveal a much higher content of oxygen-containing groups for the CNF material (9.21 *vs.* 1.9 at.%) (Figure 1d). The deconvolution of the O1s line for CNF shows that C–O and C=O functional groups predominate over –COOH groups and that the highest content corresponds to C–O functionalities. For the commercial material, no assignment could be made to -COOH groups and, similarly to the CNF electrospun material, C–O bonds predominate largely over C=O.

Raman spectra (Figure 1e), reveal typical carbon D- and G-bands located at 1345–1350 cm^{-1} and 1579 cm^{-1}, respectively, which are associated to the degree of disorder within sp^2 hybridized carbon structures (D-band), and the tangential mode of the sp^2 carbon hexagonal lattice (G-band). When comparing the intensity ratio of the D and G bands (I_D/I_G), a higher proportion of defects (or sp^3 C content) is observed for the electrospun CNF carbon nanofibers, well in agreement with the higher amount of oxygen moieties observed through XPS. Additionally, both G and D peaks are less resolved for the CNF fibers, suggesting a lower level of graphitization. As previously reported, [29] the aromatic units in lignin are randomly distributed along the chains and separated by aliphatic connectors, and this characteristic has been pointed out to contribute to low graphitization degrees even after high temperature annealing. Functionalization of carbons with oxygen-containing groups has been widely studied as an effective alternative to enhance the number of active redox sites [30][9][31][32]. This is usually manifested in higher energy efficiencies and lower activation overpotentials in VRFB due to an improvement both in the wettability and the kinetic response of the electrodes.

X-ray computed tomography (CT) was carried out to assess the morphology of the pristine samples and enable calculation of the void space fraction, tortuosity and void and fiber diameter in 3D (Figure 2). Due to the difference in scale of fiber size between the GDL 29AA and CNF samples, micro-CT was used for the former and nano-CT for the latter, both to resolve the features fully and to give the most representative volumes possible for both samples [22]. For the CNF sample, some elongated spherical nodules can be seen on some of the fibers, as well as a very large sphere towards the top surface of the mat that has caused some delamination in the material in this region. For this reason, a

sub-volume of the full scan was created for more representative analysis (Figure S1d) of the fiber and void phases.

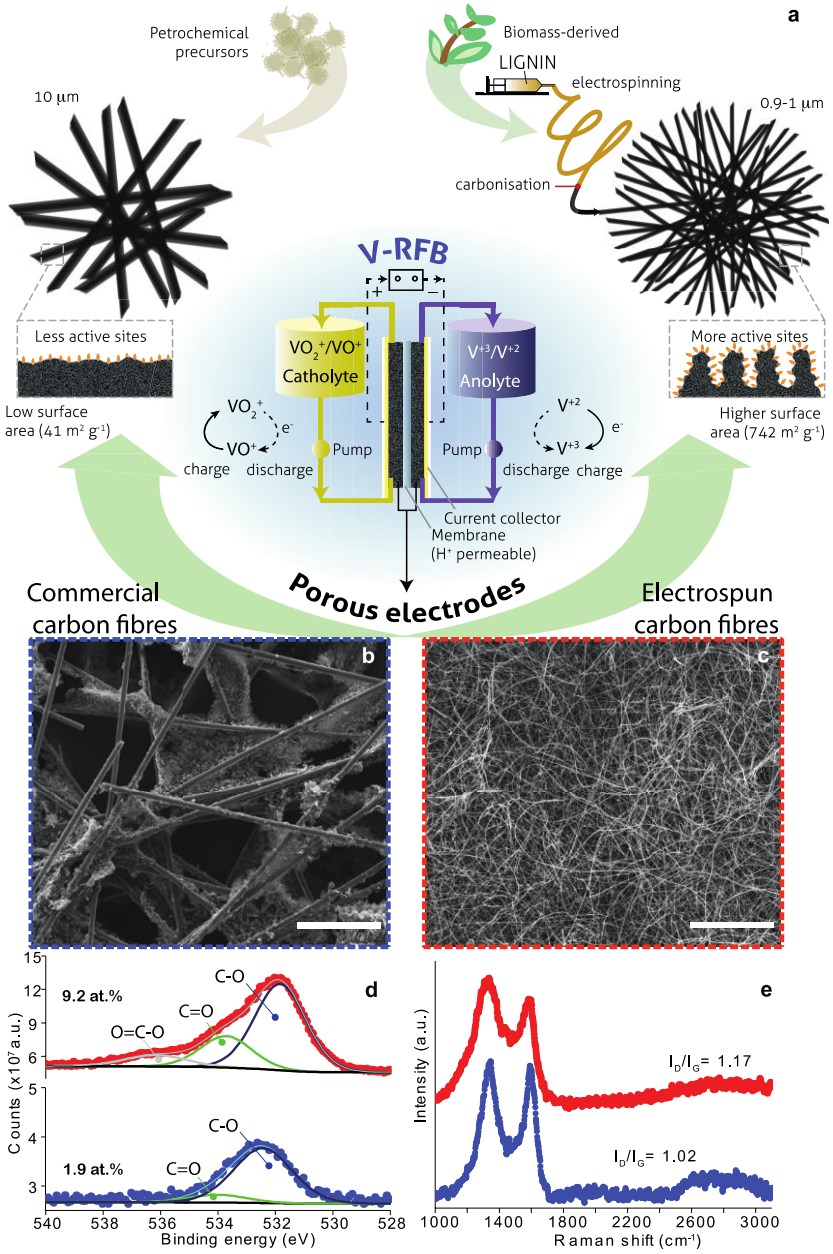

Figure 1. a) Scheme comparing a high surface area, sustainable electrospun carbon electrode material with a commercial fibrous non-woven carbon paper for their application in VRFB. SEM images of both studied materials: **b)** Commercial Sigracet® GDL29AA and **c)** CNF electrospun carbon nanofiber mat; scale bars correspond to 100 µm; **d)** Room temperature XPS spectra of the O1s line for GDL29AA (blue, bottom) and CNF (red, top); **e)** Raman spectra for GDL29AA (blue, bottom) and CNF (red, top).

The fiber diameter can be seen in the histograms in Figure S2 (top). Two distinct regions can be seen, the smaller diameters representing the majority of the fibers that have a diameter of ~ 750-1000 nm, and a minority of fibers that contain some much larger elongated spheroid features. These features are commonly seen in samples prepared *via* electrospinning, and are attributed to occasional instabilities of the Taylor cone during the electrospinning process. The volume specific surface area of the whole electrospun scan volume is 2.8 μm^{-1}, and for the sub volume, 4.0 μm^{-1} (where the influence of the large sphere is not present). The void fraction of the sub volume is 93.3 % and mean void diameter is 5.27 µm, around five times that of the fiber diameter. The fiber and void diameter were calculated using a local thickness method described elsewhere [21]. The in-plane tortuosity was found to be 1.037 and the through plane 1.048. These very low values are consistent with the expected values for highly porous fibrous media.

Micro-CT of GDL29AA shows a fiber diameter of around 7 µm and reveals large voids that are partially filled with flake-like carbon particles (seen in more detail in the nano-CT scan, Figure 2b inset). Analysis of the CT data showed the mean pore diameter to be 75 µm (Figure S3). The volume specific surface area is significantly smaller for the GDL (0.79 μm^{-1}) than the CNFs, despite the presence of the flakes, as would be expected from the larger features in comparison with the small fibers in the electrospun material (with the caveat that scanning at lower resolution will always produce a lower surface area due to fractal effects in the detail observed). More details on the XCT study of the GDL29AA are shown in Figure S4.

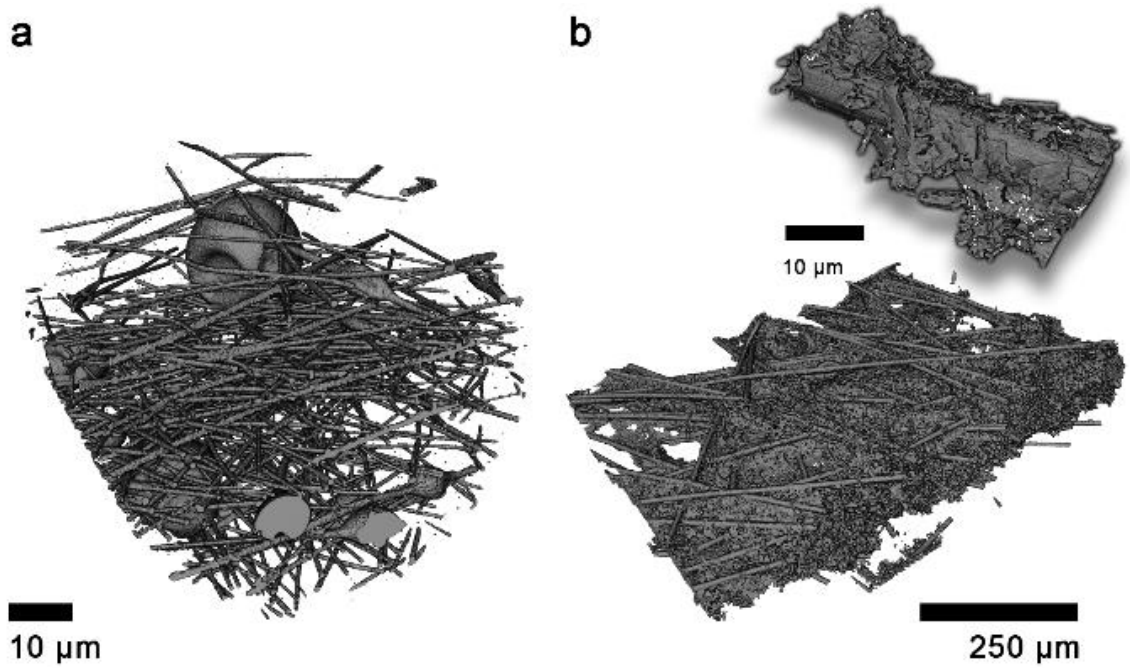

Figure 2. X-ray nano-CT of the CNF electrode (a) and micro-CT of the GDL29AA (b), including a nano-CT view of a single fiber showing the flake-like structure of the material between the fibers (b, inset).

With the aim of further enhancing the electrocatalytic activity of the studied electrodes towards both redox reactions of vanadium (V^{3+}/V^{2+} and VO_2^+/VO^{2+}), phosphate functional groups were introduced through the thermal decomposition of NH_4PF_6 [26]. As previously reported, this treatment leads to oxygen-enriched surfaces, as every phosphate group contributes with three new oxygen centers.

After phosphorous doping, the microstructure of samples remained unaltered (Figure S5) while the BET surface area and chemistry changed drastically. The BET surface area of the CNF electrode suffered the highest decrease, with a value of 27 m^2 g^{-1} for the P-doped material (Table S1). We attribute this observation to micro and mesopore blockage upon doping, which was only observed for our CNF sample, as the commercial GDL29AA has no initial microporosity. BET reduction is discernible only with the N_2 sorption isotherm but not with CO_2. Since CO_2 has a higher electric quadrupole moment than N_2, it is expected to interact more strongly with polar surface groups that would arise after doping, such as $-PO_3$ or C=O. Hence, the CO_2 sorption shown in Table S2 shows the opposite trend.

With regard to the chemistry, as observed in Figure 3, XPS profiles of both P-doped samples show the presence of the P2p peak, between 144 and 126 eV. This band was deconvoluted into the $2p_{3/2}$ and $2p_{1/2}$ spin-orbit components displaying a 1:2 intensity ratio. As shown in both spectra, our best fit accounted for two P environments, P-O and P-C, in good correlation with the C-O content observed in the XPS O1s and C1s spectra of the P-doped samples (Figures S6, S7 and S8). Since the mechanism of phosphate doping has been proposed to occur *via* condensation of the carbons´ surface –OH groups and the phosphate ions, it is not surprising that the P-doped CNF sample shows a much higher overall P content (2.8 *vs.* 0.18 at.%), in agreement with its higher amount of initial oxygen functionalities (9.2 *vs.* 1.9 at%).

P-doping with NH_4PF_6 was expected to increase also the amount of Nitrogen in the doped samples, as corroborated in Figure 3c and 3d. When comparing the trends, as in the case of phosphorus, the incorporation of Nitrogen in our electrospun material resulted in more prominent N peaks in the high resolution XPS and, importantly, we observed the appearance of a slight shoulder at higher binding energies for the electrospun material which was not present in the GDL29AA samples. This band could be assigned to polar N-H functionalities, which, in accordance to the presence of -COOH groups only in the CNF sample, could have formed from the decomposition of NH_4^+ and the subsequent reaction with the acid functionalities.

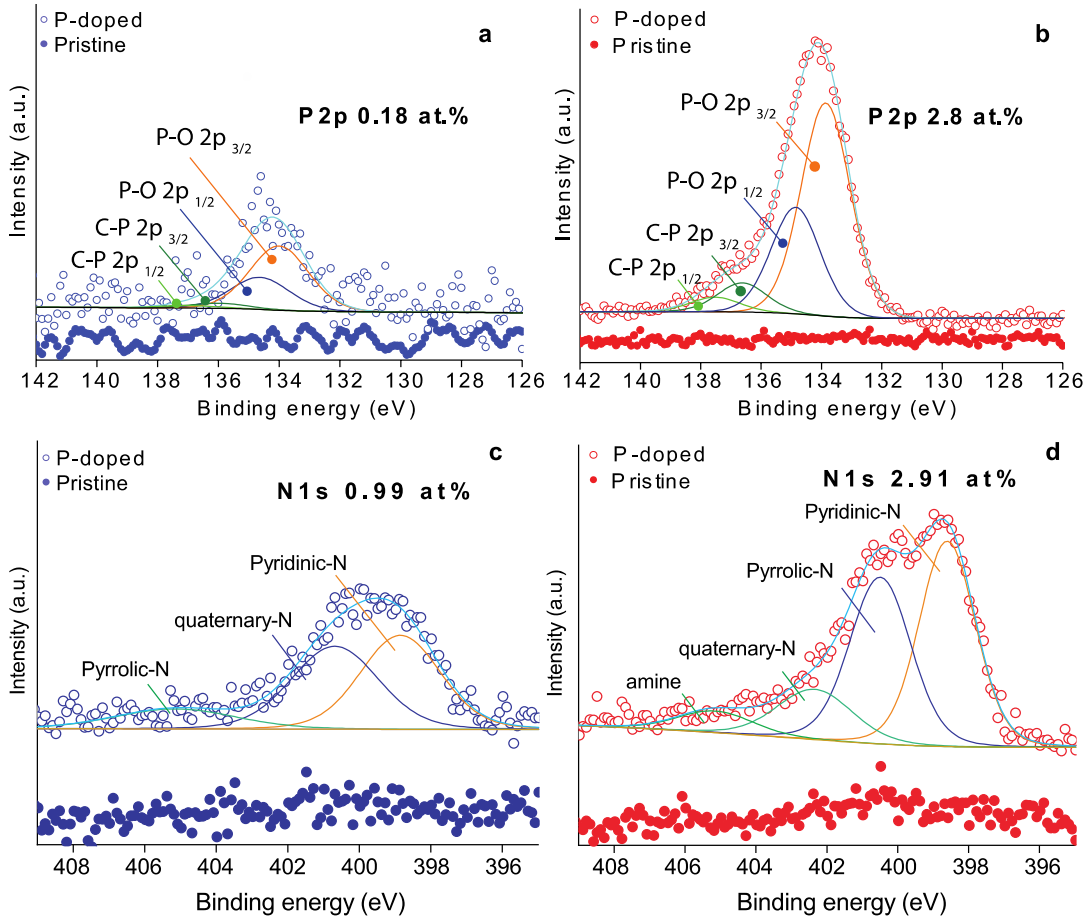

Figure 3. XPS analysis (solid symbols: pristine, open symbols: P-doped) of the P-bands: **a)** GDL29AA (solid symbols: pristine, open symbols: P-doped) and **b)** CNF; and the N-bands: **c)** GDL29AA and **b)** CNF.

The O1s XPS bands of both materials before and after the introduction of -PO_3 groups for both GDL29AA and CNF are shown in Table 1 (see Table S3 for complete XPS quantification). Due to the similar binding energies, discerning between C-O/P-O, C=O/P=O bonds [33] can be challenging. However, it is possible to split the O1s band into three different regions [34]: **a)** 535.6-536.49 eV corresponding to C=O/O-P=O, **b)** between 532.8 and 5.33.9 eV, for C-O/C-O-P bonds and **c)** 531.7-532.82 eV for C=O/P=O. Our best fits for all three regions of the O1s band for each sample indicate the appearance of two new peaks that were attributed to P-O and P=O bonds.

For both materials, a shift to higher binding energies upon doping for the C-O band is observed (*e.g.* from 532.8 to 533.1 eV for CNF and from 532.7 to 532.93 eV for GDL29AA), suggesting a change

in the environment of the initial –OH functionalities. In contrast, the C=O band which is not expected to be affected by the introduction of new -PO_3 groups remains mostly unaltered. The appearance of P=O and P-O groups upon the doping treatment is concomitant with the reduction of the at.% of both C-O and C=O bonds, thus suggesting the parallel consumption of C-OH for the -PO_3 introduction and the release of C=O bonds. It is worth mentioning that the decrease of this band is only minor for the GDL29AA material, while much more considerable for our electrospun CNF mat. Additionally, the percentage of O-C=O bonds decreases dramatically as well upon doping. We believe that this could be attributed to the thermal lability of such groups, in agreement with the previous observations made through Raman spectroscopy.

Table 1. XPS survey on the composition of the O1s bands.

		O 1s composition				
	O 1s	***O= C***	***O=P***	***O-C***	***O-P***	***O-C=O***
Sample	**Tot. at.%**	at.% (eV) [a]	at.% (eV) [a]	at.% (eV) [a]	at.% (eV) [a]	at.% (eV) [a]
CNF	9.22	24 (533.7)	-	65.7 (531.8)	-	10.3 (536.2)
CNF P-doped	10.09	9.5 (533.5)	39.8 (533.1)	28.2 (531.3)	19.4 (532.3)	3.1 (535.9)
GDL29AA	1.92	12.2 (534.0)	-	87.8 (532.4)	-	-
GDL29AA P-doped	2.47	8.5 (534.0)	42.4 (533.0)	28.0 (531.5)	21.2 (532.2)	-

[a] Fractions of C=O, C-O and O-C=O species from fits of the O1s region. Position of peaks after deconvolution are shown in brackets.

With regard to the alteration of the sp^2-C lattice, no clear shifts were observed in the Raman bands after doping, (Figure S9) while the I_D/I_G ratio slightly decreased only for the P-doped CNF sample when compared to the pristine one.

3.2 Half-cell performance: Electrochemical characterization

Cyclic voltammograms (CV) (Figures 4a and b) conducted between -0.1 and 1.2 V (*vs.* SCE) show the characteristic anodic and cathodic current peaks observed for the redox reactions that vanadium undergoes on the surface of the electrodes:

$$VO_2^+ + 2H^+ + e^- \leftrightarrow VO^{2+} + H_2O \qquad E^0 = 1.00\,V\ vs.RHE \qquad (1)$$

$$VO^{2+} + 2H^+ + e^- \leftrightarrow V^{3+} + H_2O \qquad E^0 = 0.34\,V\ vs.RHE \qquad (2)$$

$$V^{3+} + e^- \leftrightarrow V^{2+} \qquad E^0 = -0.26\,V\ vs.RHE \qquad (3)$$

V^{3+}/V^{2+} peaks are superimposed on the negative current generated by HER (caused by the Pt current collector used in the half cell, three-electrode set up), therefore CV analysis was done through the VO^{2+}/VO_2^+ reaction peaks (between ~0.7 and 1.2V). Figure 4 shows the CV of the two materials in a V(III)/V(VI) mixed electrolyte, including an example CV of the bare Pt electrode (black). It is clear from the Pt CV that there is very little current contribution in the region of the $V^{4+/5+}$ peak (at positive potentials), whereas the Pt contributes to the HER at negative potentials, obscuring any $V^{2+/3+}$ redox couple. Therefore, for the purposes of the CV activity of these materials we consider only the $V^{4+/5+}$

couple n this electrochemical set up. It is evident that the pristine CNF sample outperforms the commercial GDL29AA, as both cathodic and anodic current densities show higher values when normalized to geometric area. In the case of GDL29AA, P-doping seems to modestly favor the VO^{2+}/VO_2^{+} reaction, as peaks become slightly sharper and ΔV (cathodic – anodic) decreases [26]. Unexpectedly, for the P-doped CNF sample, the peaks become less intense and ΔV increases. This suggests that the strategy to enhance the number or active sites through the introduction of phosphate groups in these lignin-derived carbon fibers, that already had a high content of oxygen functionalities, is counterproductive. We hypothesize that the newly introduced bulky phosphate groups, generated over –OH functionalities might be hindering the activity of adjacent C=O oxygen centers that need neighboring groups to activate a chelating-type of catalytic performance [35]. Furthermore, as previously mentioned, the drastic decrease in BET surface area for the CNF sample after doping suggests pore blockage, which in turn would lead to fewer reactive sites available for Vanadium ions. In the case of GDL29AA, surface area for the pristine material is already extremely low, therefore treatment with NH_4PF_6 results in doping without the detrimental effect of pore blockage.

Additionally, the content of -O-C=O groups also decreases upon P-doping for the CNF sample and that might suggest that these acidic groups play a determinant mechanistic role in the redox chemistry of Vanadium [36][37]. Further investigation is currently being conducted to understand the mechanism with the different types of oxygen functionalities, as it has been already suggested that each type of oxygen activates the surface in very dissimilar ways [38].

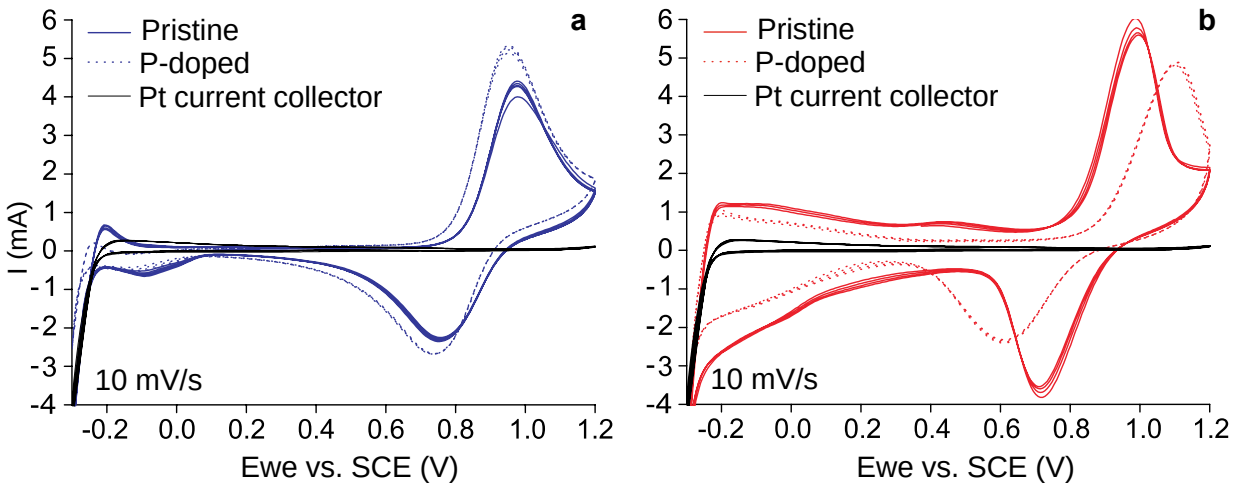

Figure 4. Cyclic voltammograms for samples with exposed areas of 0.79mm^2 for: **a)** GDL29AA (solid lines: blue: pristine, black: Pt current collector, dashed lines: P-doped) and **b)** CNF (solid lines: red: pristine, black: Pt current collector, dashed lines: P-doped).

3.3 Full cell performance: Polarization curve and cyclability tests

The fibrous mats were also evaluated in a full RFB cell, where no Pt current collectors exist to obscure the activity of the negative redox couple. To evaluate the kinetic cell potential variations due to different sources of polarization (e.g. activation overpotential, mass transference, concentration polarisation, ohmic polarization) [39] we recorded the cell voltage at different current densities as shown in the polarization curves at 100% State of Charge (SoC) in Figure 5. All profiles show almost linear decays with current density, which suggests polarization mainly related to the conductivity of samples. There seems to be similar losses for all systems, with P-doped CNF showing the worst performance, in agreement with the poorer kinetic redox performance observed for this sample in three-electrode cell CVs (Figure 4b). In the case of the commercial GDL29AA samples, both pristine and P-doped electrodes behave very similarly, although the P-doped sample shows slightly lower voltage retention at higher current densities.

Contrary to what the results obtained using the half-cells suggested, the CNF electrode shows greater polarization losses than the commercial one in a full-cell configuration. We believe this could be due to electrolyte flow inhomogeneity within the electrode, which will be more prominent for the

electrospun samples, as has been shown in previous fluid dynamics simulations in electrospun flow battery mats [21][22]. This can be corroborated by the slightly higher voltage drop observed at higher current densities, as the effect of the hindered electrolyte permeability is more noticeable precisely at high current densities or when larger fractions of electrode are used [40]. Additionally, electrospun materials with a low degree of graphitization and poor through-plane fiber contact will be expected to have significantly lower electrical conductivity than those of commercially available GDL fibers, graphitized at high temperatures. Accordingly, when electrical conductivity was measured across the assembled electrode layers, values showed the following trend: Pristine GDL29AA > P-doped GDL29AA > Pristine CNF > P-doped CNF (25.3 > 19.6 > 9.8 > 2.6 S m^{-1}). In spite of having lower conductivity values, it is worth mentioning that the behavior of our pristine electrospun material is comparable to that observed for the commercial ones. This suggests that improvements to and optimization of the carbonization process could mean that the lignin-based materials could surpass the performance of the commercial standard. Additionally, further optimization of the flow cell experimental parameters for the electrospun mats should improve their performance compared with the commercial materials. In fact, given the significantly lower conductivity (nearly an order of magnitude difference between the P-doped CNF and pristine GDL29AA) shown for the electrospun materials, it is remarkable that they obtain similar performance in the initial cycles of full cell testing, suggesting that despite the limitations of low electrical conductivity, these materials possess inherent catalytic / surface properties that could be even more beneficial for VRFBs once optimization increases the conductivity.

Interestingly, both P-doped samples showed lower conductivities that the pristine forms, which might be associated to the generation of surface N/P-defects upon doping. This would prevent inter-fiber electron tunneling but at the same time would increase the number of electrocatalytic sites for Vanadium redox reactions.

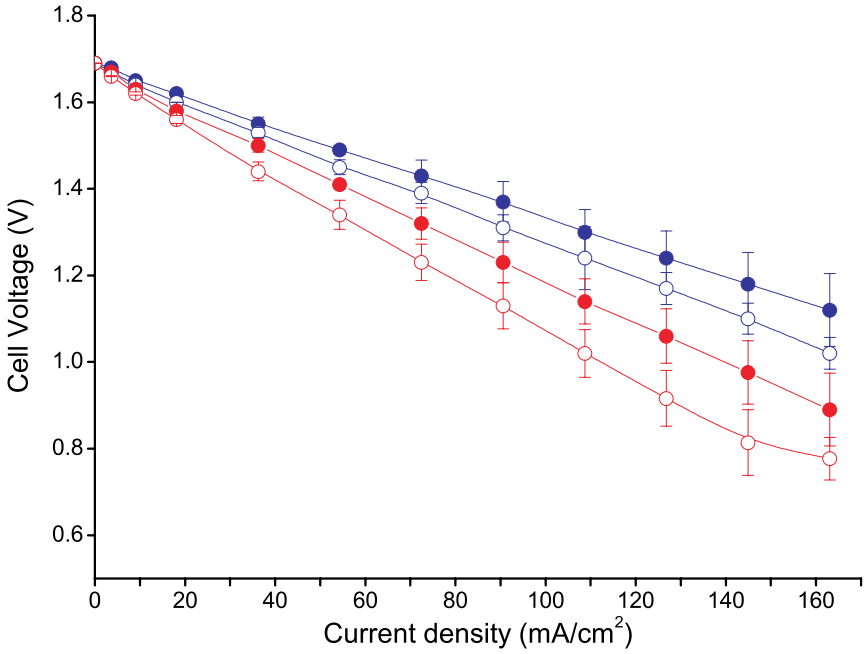

Figure 5. Polarization curves for: GDL29AA (blue, solid symbols: pristine, void symbols: P-doped) and CNF (red, solid symbols: pristine, void symbols: P-doped).

The cell voltage *vs.* time for all samples is presented in Figure 6. In the case of the pristine samples, both keep steady charge-discharge profiles throughout all cycles. However, P-doped samples start deviating from their pristine analogues as soon as in the second charge-discharge cycle, which suggests these samples might be promoting side reactions and thus, shifting the cell balance and effectively lowering the capacity of the battery.

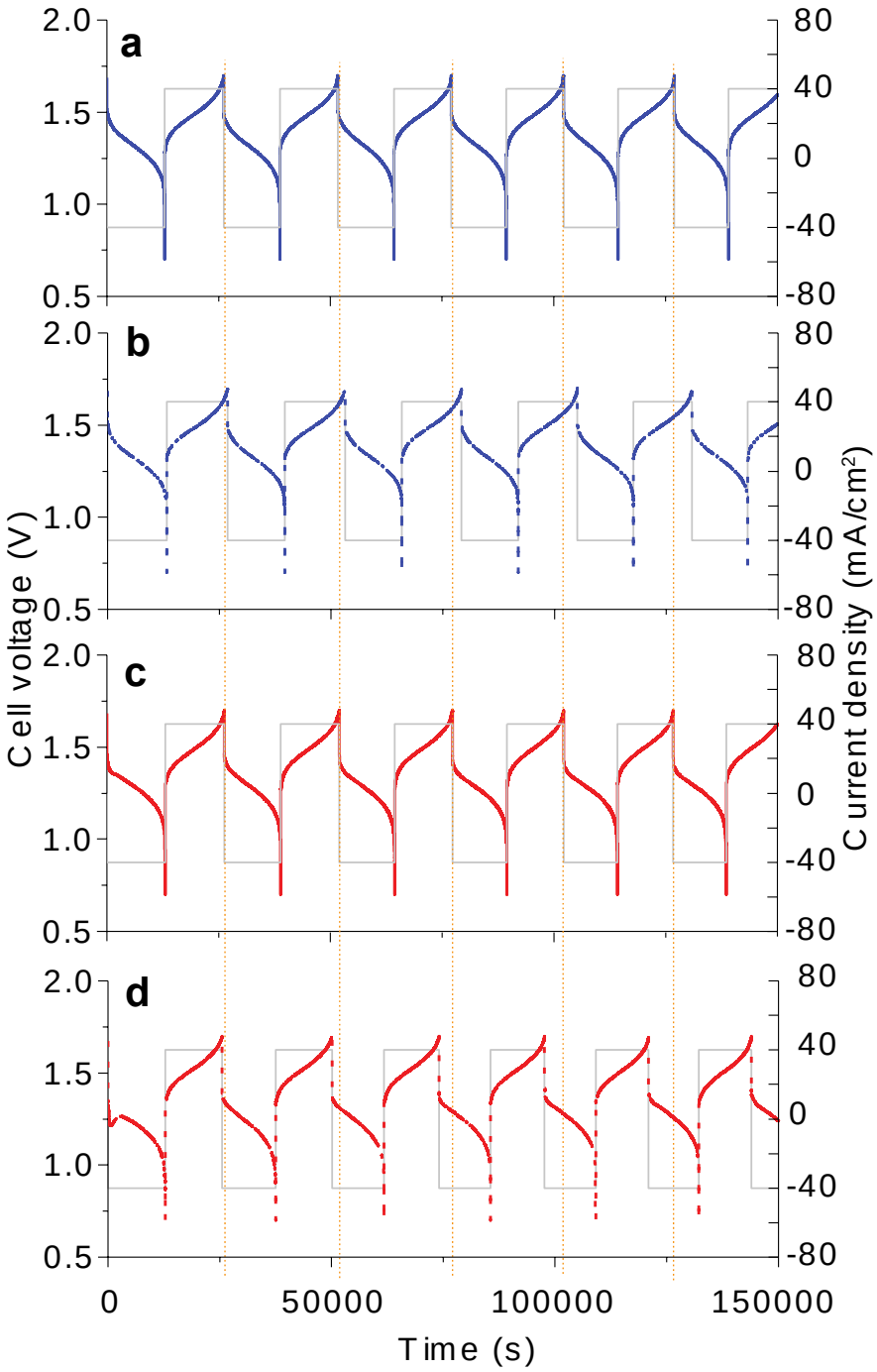

Figure 6. Cyclability tests showing the variations observed within the 5 first cycles for: **a)** pristine GDL29AA, **b)** P-doped GDL29AA, **c)** pristine CNF and **d)** P-doped CNF.

The cell capacity and energy efficiency are plotted for 15 cycles at a current density of 40 mA/cm^2 in Figure 7 (theoretical capacity is 21.4 Ah/L using a 1.6 M electrolyte concentration and two 20 mL reservoirs). Capacity fades for all samples, although more prominently for P-doped samples. In

accordance to the previous observations, P-doping seems to provoke unwanted reactions between the electrodes and the electrolyte, thus decreasing the usable capacity with time and altering the time for charge/discharge. This is also seen by the values of Coulombic efficiency in Figure 7b, which are not particularly high, thus suggesting side reactions are interfering with the performance of our electrospun materials, most likely HER at the negative electrode. However, there is no need for the electrodes in RFBs to be symmetrical, where the same material is used for the negative and the positive electrodes. So though these materials may not be optimized for the negative electrode, paired with a different material they could have potential as positive electrodes in VRFBs, as well as having room for optimization of the microstructure and surface chemistry.

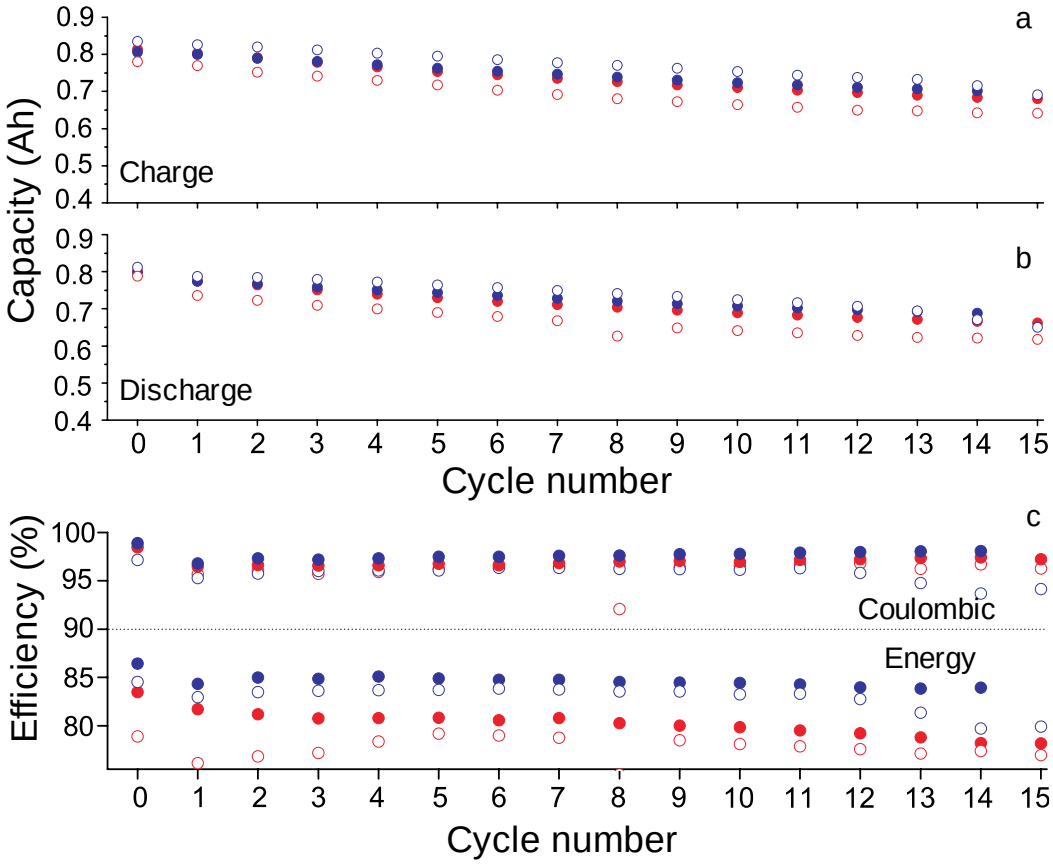

Figure 7. Cell capacity charge **(a)** and discharge **(b)**, and cell efficiency **(c)** for: GDL29AA (blue, solid symbols: pristine, void symbols: P-doped) and CNF (red, solid symbols: pristine, void symbols: P-doped).

4. Conclusions

In this work, we have compared the suitability of biomass-derived electrospun mats as electrodes for RFBs with commercially available carbon papers, and have tested for the first time a lignin-derived carbon electrode in a full redox flow cell. Characterization of the electrodes shows significant differences in their morphology and surface characteristics, leading to diversion of performance in operating flow batteries. P-doping was hypothesized to increase the activity towards the redox couples, which showed a slight positive effect for the GDL, but a negative effect for the CNF in a three-electrode electrochemical test, possibly mainly due to loss of active sites and surface area. Additionally, the performance in a full cell seemed to be slightly hindered by the P-doping for both samples. Nevertheless, there is significant room for improvement in both morphology and surface chemistry for electrospun fibers, allowing control and optimization of porosity, fiber size, surface functionality and conductivity. Tuning these factors could see sustainably derived electrospun carbons out-performing commercial materials in the near future.

Acknowledgements

The authors ABJ, RJ and MCR thank the CAM-IES for funding (EP/P007767/1). ABJ also thanks the Engineering and Physical Sciences Research Council for financial support (EP/P031323/1). PLC thanks the EPSRC for support via his fellowship, EP/S001298/1. LG thanks Erasmus+ traineeship program for funding received to support research placement (2018-IE02-KAI03-000579). PRS acknowledges funding from the Royal Academy of Engineering.

Keywords: Redox-flow batteries • bio-sustainable carbons • energy conversion • carbon electrodes• vanadium electrochemistry

References

[1] IPPC, Climate Change 2013: The Physical Science Basis. Working Group I Contribution to

the Fifth Assessment Report of the Intergovernmental Panel on Climate Change [Stocker, T.F., D. Qin, G.-K. Plattner, M. Tignor, S.K. Allen, J. Boschung, A. Nauels, Y. Xia, V., Cambridge Univ. Press. Cambridge, United Kingdom New York, NY, USA. (2013) 1535. doi:10.1029/2001JD001516.

[2] P. Cappers, J. MacDonald, C. Goldman, O. Ma, An assessment of market and policy barriers for demand response providing ancillary services in U.S. electricity markets, Energy Policy. 62 (2013) 1031–1039. doi:10.1016/J.ENPOL.2013.08.003.

[3] J. Winsberg, T. Hagemann, T. Janoschka, M.D. Hager, U.S. Schubert, Redox-Flow Batteries: From Metals to Organic Redox-Active Materials, Angew. Chemie - Int. Ed. 56 (2017) 686–711. doi:10.1002/anie.201604925.

[4] C. Choi, S. Kim, R. Kim, Y. Choi, S. Kim, H. Jung, J.H. Yang, H.-T. Kim, A review of vanadium electrolytes for vanadium redox flow batteries, Renew. Sustain. Energy Rev. 69 (2017) 263–274. doi:10.1016/J.RSER.2016.11.188.

[5] C. Liuyue, S.-K. Maria, W. Dawei, Electrode modification and electrocatalysis for redox flow battery (RFB) applications, Energy Storage Sci. Technol. 4 (2015) 433–457. doi:10.3969/J.ISSN.2095-4239.2015.05.001.

[6] M. Skyllas-Kazacos, L. Cao, M. Kazacos, N. Kausar, A. Mousa, Vanadium Electrolyte Studies for the Vanadium Redox Battery-A Review, ChemSusChem. 9 (2016) 1521–1543. doi:10.1002/cssc.201600102.

[7] Z.H. Zhang, T.S. Zhao, B.F. Bai, L. Zeng, L. Wei, A highly active biomass-derived electrode for all vanadium redox flow batteries, Electrochim. Acta. 248 (2017) 197–205. doi:10.1016/J.ELECTACTA.2017.07.129.

[8] W. Lu, X. Li, H. Zhang, The next generation vanadium flow batteries with high power density – a perspective, Phys. Chem. Chem. Phys. 20 (2018) 23–35.

doi:10.1039/C7CP07456E.

[9] C. Flox, M. Skoumal, J. Rubio-Garcia, T. Andreu, J.R. Morante, Strategies for enhancing electrochemical activity of carbon-based electrodes for all-vanadium redox flow batteries, Appl. Energy. 109 (2013) 344–351. doi:10.1016/J.APENERGY.2013.02.001.

[10] K.J. Kim, M.-S. Park, Y.-J. Kim, J.H. Kim, S.X. Dou, M. Skyllas-Kazacos, A technology review of electrodes and reaction mechanisms in vanadium redox flow batteries, J. Mater. Chem. A. 3 (2015) 16913–16933. doi:10.1039/C5TA02613J.

[11] D. Aaron, Z. Tang, A.B. Papandrew, T.A. Zawodzinski, Polarization curve analysis of all-vanadium redox flow batteries, J. Appl. Electrochem. 41 (2011) 1175–1182. doi:10.1007/s10800-011-0335-7.

[12] L. Zhang, A. Aboagye, A. Kelkar, C. Lai, H. Fong, A review: carbon nanofibers from electrospun polyacrylonitrile and their applications, J. Mater. Sci. 49 (2014) 463–480. doi:10.1007/s10853-013-7705-y.

[13] F. Tariq, J. Rubio-Garcia, V. Yufit, A. Bertei, B.K. Chakrabarti, A. Kucernak, N. Brandon, Uncovering the mechanisms of electrolyte permeation in porous electrodes for redox flow batteries through real time *in situ* 3D imaging, Sustain. Energy Fuels. 2 (2018) 2068–2080. doi:10.1039/C8SE00174J.

[14] S. Herou, P. Schlee, A.B. Jorge, M. Titirici, Biomass-derived electrodes for flexible supercapacitors, Curr. Opin. Green Sustain. Chem. 9 (2018) 18–24. doi:10.1016/J.COGSC.2017.10.005.

[15] J. Vivo-Vilches, A. Celzard, V. Fierro, I. Devin-Ziegler, N. Brosse, A. Dufour, M. Etienne, J.F. Vivo-Vilches, A. Celzard, V. Fierro, I. Devin-Ziegler, N. Brosse, A. Dufour, M. Etienne, Lignin-Based Carbon Nanofibers as Electrodes for Vanadium Redox Couple Electrochemistry, Nanomaterials. 9 (2019) 106. doi:10.3390/nano9010106.

[16] P. Schlee, S. Herou, R. Jervis, P.R. Shearing, D.J.L. Brett, D. Baker, O. Hosseinaei, P. Tomani, M.M. Murshed, Y. Li, M.J. Mostazo-López, D. Cazorla-Amorós, A.B. Jorge Sobrido, M.-M. Titirici, Free-standing supercapacitors from Kraft lignin nanofibers with remarkable volumetric energy density, Chem. Sci. 10 (2019) 2980–2988. doi:10.1039/C8SC04936J.

[17] G. Wei, X. Fan, J. Liu, C. Yan, A review of the electrochemical activity of carbon materials in vanadium redox flow batteries, Carbon N. Y. 81 (2015) 850. doi:10.1016/J.CARBON.2014.08.032.

[18] Suhas, P.J.M. Carrott, M.M.L. Ribeiro Carrott, Lignin – from natural adsorbent to activated carbon: A review, Bioresour. Technol. 98 (2007) 2301–2312. doi:10.1016/J.BIORTECH.2006.08.008.

[19] J. Roman, W. Neri, A. Derré, P. Poulin, Electrospun lignin-based twisted carbon nanofibers for potential microelectrodes applications, Carbon N. Y. 145 (2019) 556–564. doi:10.1016/J.CARBON.2019.01.036.

[20] P. Schlee, O. Hosseinaei, D. Baker, A. Landmér, P. Tomani, M.J. Mostazo-López, D. Cazorla-Amorós, S. Herou, M.-M. Titirici, From Waste to Wealth: From Kraft Lignin to Free-standing Supercapacitors, Carbon N. Y. 145 (2019) 470–480. doi:10.1016/J.CARBON.2019.01.035.

[21] M.D.R. Kok, R. Jervis, D. Brett, P.R. Shearing, J.T. Gostick, Insights into the Effect of Structural Heterogeneity in Carbonized Electrospun Fibrous Mats for Flow Battery Electrodes by X-Ray Tomography, Small. 14 (2018) 1–15. doi:10.1002/smll.201703616.

[22] R. Jervis, M.D.R. Kok, J. Montagut, J.T. Gostick, D.J.L. Brett, P.R. Shearing, X-ray Nano Computed Tomography of Electrospun Fibrous Mats as Flow Battery Electrodes, Energy Technol. 6 (2018) 2488–2500. doi:10.1002/ente.201800338.

[23] M.D.R. Kok, R. Jervis, T.G. Tranter, M.A. Sadeghi, D.J.L. Brett, P.R. Shearing, J.T. Gostick, Mass transfer in fibrous media with varying anisotropy for flow battery electrodes: Direct numerical simulations with 3D X-ray computed tomography, Chem. Eng. Sci. 196 (2019) 104–115. doi:10.1016/J.CES.2018.10.049.

[24] R. Moerck, H. Yoshida, K.P. Kringstad, H. Hatakeyama, Holzforschung., 1986. http://agris.fao.org/agris-search/search.do?recordID=DE87T0653 (accessed March 8, 2019).

[25] R. Moerck, H. Yoshida, K.P. Kringstad, H. Hatakeyama, High Glass Transition Lignins and Lignin Derivatives for the Manufacture of Carbon and Graphite Fibers, (2014). https://patents.google.com/patent/US20140271443A1/en (accessed March 8, 2019).

[26] K.J. Kim, H.S. Lee, J. Kim, M.S. Park, J.H. Kim, Y.J. Kim, M. Skyllas-Kazacos, Superior electrocatalytic activity of a robust carbon-felt electrode with oxygen-rich phosphate groups for all-vanadium redox flow batteries, ChemSusChem. 9 (2016) 1329–1338. doi:10.1002/cssc.201600106.

[27] A. Tkachuk, F. Duewer, H. Cui, M. Feser, S. Wang, W. Yun, X-ray computed tomography in Zernike phase contrast mode at 8 keV with 50-nm resolution using Cu rotating anode X-ray source, Zeitschrift Für Krist. - Cryst. Mater. 222 (2007) 650–655. doi:10.1524/zkri.2007.222.11.650.

[28] O.O. Taiwo, D.P. Finegan, J. Gelb, C. Holzner, D.J.L. Brett, P.R. Shearing, The use of contrast enhancement techniques in X-ray imaging of lithium–ion battery electrodes, Chem. Eng. Sci. 154 (2016) 27–33. doi:10.1016/J.CES.2016.04.023.

[29] P. Langan, A.K. Naskar, F. Chen, M.J. Biddy, C.E. Wyman, P. Gilna, B.H. Davison, J.N. Saddler, R.A. Dixon, T.J. Tschaplinski, M.F. Davis, M. Keller, G.A. Tuskan, R. Chandra, G.T. Beckham, A.J. Ragauskas, Lignin Valorization: Improving Lignin Processing in the Biorefinery, Science (80-.). 344 (2014) 1246843–1246843. doi:10.1126/science.1246843.

[30] K.J. Kim, S.-W. Lee, T. Yim, J.-G. Kim, J.W. Choi, J.H. Kim, M.-S. Park, Y.-J. Kim, A new strategy for integrating abundant oxygen functional groups into carbon felt electrode for vanadium redox flow batteries, Sci. Rep. 4 (2015) 6906. doi:10.1038/srep06906.

[31] D.M. Kabtamu, J.Y. Chen, Y.C. Chang, C.H. Wang, Water-activated graphite felt as a high-performance electrode for vanadium redox flow batteries, J. Power Sources. 341 (2017) 270–279. doi:10.1016/j.jpowsour.2016.12.004.

[32] Y. Huang, Q. Deng, X. Wu, S. Wang, N, O Co-doped carbon felt for high-performance all-vanadium redox flow battery, Int. J. Hydrogen Energy. 42 (2017) 7177–7185. doi:10.1016/j.ijhydene.2016.04.004.

[33] F.J. García-Mateos, R. Berenguer, M.J. Valero-Romero, J. Rodríguez-Mirasol, T. Cordero, Phosphorus functionalization for the rapid preparation of highly nanoporous submicron-diameter carbon fibers by electrospinning of lignin solutions, J. Mater. Chem. A. 6 (2018) 1219–1233. doi:10.1039/C7TA08788H.

[34] L. Zhao, Natural phosphorus-doped honeycomb carbon materials as oxygen reduction catalysts derived from Pulsatilla chinensis (Bunge) Regel, RSC Adv. 7 (2017) 13904–13910. doi:10.1039/C6RA28630E.

[35] C. Noh, S. Moon, Y. Chung, Y. Kwon, Chelating functional group attached to carbon nanotubes prepared for performance enhancement of vanadium redox flow battery, J. Mater. Chem. A. 5 (2017) 21334–21342. doi:10.1039/C7TA06672D.

[36] N. Pour, D.G. Kwabi, T. Carney, R.M. Darling, M.L. Perry, Y. Shao-Horn, Influence of Edge- and Basal-Plane Sites on the Vanadium Redox Kinetics for Flow Batteries, J. Phys. Chem. C. 119 (2015) 5311–5318. doi:10.1021/jp5116806.

[37] Y. Men, T.S.-I.J.E. Sci, undefined 2012, Carbon felts electrode treated in different weak acid solutions through electrochemical oxidation method for all vanadium redox flow battery,

Electrochemsci.Org. (n.d.). http://electrochemsci.org/papers/vol7/7043482.pdf (accessed March 20, 2019).

[38] I. Mustafa, A. Al Shehhi, A. Al Hammadi, R. Susantyoko, G. Palmisano, S. Almheiri, Effects of carbonaceous impurities on the electrochemical activity of multiwalled carbon nanotube electrodes for vanadium redox flow batteries, Carbon N. Y. 131 (2018) 47–59. doi:10.1016/J.CARBON.2018.01.069.

[39] A.M. Pezeshki, J.T. Clement, G.M. Veith, T.A. Zawodzinski, M.M. Mench, High performance electrodes in vanadium redox flow batteries through oxygen-enriched thermal activation, J. Power Sources. 294 (2015) 333–338. doi:10.1016/J.JPOWSOUR.2015.05.118.

[40] S. Liu, M. Kok, Y. Kim, J.L. Barton, F.R. Brushett, J. Gostick, Evaluation of Electrospun Fibrous Mats Targeted for Use as Flow Battery Electrodes, J. Electrochem. Soc. 164 (2017) A2038–A2048. doi:10.1149/2.1301709jes.